



Gaussian process surrogate modeling for efficient controller tuning and fatigue load prediction of the helix wake-mixing method

Daan van der Hoek¹, Tim Dammann¹, and Jan-Willem van Wingerden¹

¹Delft Center for Systems and Control, Faculty of Mechanical Engineering, Delft University of Technology, Delft, The Netherlands

Correspondence: Daan van der Hoek (d.c.vanderhoek@tudelft.nl)

Abstract.

Wind farms experience reduced power production and elevated structural loading due to wake interactions. Wake-mixing control techniques, which dynamically excite upstream turbine wakes to accelerate recovery, have demonstrated promising improvements in downstream power production but at the expense of increased fatigue loading. Identifying the optimal control settings and quantifying the resulting load implications remain challenging because these methods require high-fidelity simulations that capture both the dynamic actuation and the resulting turbulence. Moreover, existing load surrogate models do not incorporate wake-mixing control, largely because conventional engineering wake models are unable to reproduce periodic wake excitation. This study presents two complementary advances to improve the design of wake-mixing strategies using a limited number of large-eddy simulations (LES) and Gaussian process (GP) regression. First, we develop an efficient simulation-driven framework to identify optimal frequency and amplitude parameters for wake-mixing control, yielding a clear optimal power gain of 7.5% near a Strouhal number of 0.25 and pitch amplitudes of around 4° for a two-turbine array. Second, we present a surrogate model capable of predicting fatigue loads for wake-mixing control. Using LES-derived rotor-plane inflow fields for aeroelastic simulations, we construct a load database that encompasses various combinations of wake overlap, turbine spacing, and wind farm control settings. The result is a load surrogate model based on GP regression trained on sector-averaged inflow quantities that accurately predicts damage equivalent loads, including the effect of increased excitation in the wake. This model enables the joint evaluation of power gains and load penalties at the wind farm level, supporting a more informed design of wake-mixing control strategies.

1 Introduction

Wind farms that are densely spaced suffer from power production losses and increased structural loads as wind turbines are, at times, subject to turbulent wakes (Meyers et al., 2022). The field of wind farm flow control (WFFC) attempts to minimize the negative implications of the wake effect by altering the wake to improve power efficiency or reduce fatigue loading. Wind farm flow control methods can be categorized in three groups. First, static induction control (SIC) tries to reduce the velocity deficit and turbulence intensity in the wake by altering one of the steady-state operating setpoints (generally the pitch angle or tip-speed ratio) of a turbine (Kanev et al., 2018). Effectively, this method more evenly redistributes the power output and loading



25 over multiple turbines, without significantly improving the overall wind farm performance (van der Hoek et al., 2019). Second, wake steering control adds an additional control variable to the turbine in the form of a yaw misalignment. This misalignment of the turbine with the dominant wind direction introduces a lateral component of the thrust force acting on the incoming flow, resulting in a wake that is steered away from downstream turbines (Fleming et al., 2014; Gebraad et al., 2016). While a yaw misalignment reduces the energy production of a wind turbine, downstream turbines benefit from higher inflow velocities and
30 can improve the combined power output of the wind farm. Last, for wake-mixing control, upstream turbines are dynamically actuated to excite the wake and trigger wake recovery mechanisms at an earlier stage. This is generally achieved by feeding a periodic reference signal for collective pitch control (Munters and Meyers, 2018b), individual pitch control (Frederik et al., 2020a), or yaw control (Munters and Meyers, 2018a).

Unlike WFFC methods that adjust a static control setpoint such as SIC or wake steering, the effectiveness of wake-mixing
35 techniques also relies on the amplitude and frequency of excitation. Where steady-state wind farm simulation tools like FLORIS (NREL, 2024) or PyWake (Pedersen et al., 2023) are generally used to optimize yaw angles and induction factors, the optimal frequency and amplitude for wake-mixing methods are obtained through high-fidelity models such as large eddy simulations (LES). Initial studies on periodic dynamic induction control indicated an optimal frequency for a Strouhal number of $St = 0.25$ (Munters and Meyers, 2018b). The dimensionless Strouhal number is expressed as $St = f_e \cdot D / U_\infty$,
40 with excitation frequency f_e , rotor diameter D , and inflow velocity U_∞ . Successive simulation studies (Frederik et al., 2020a; Muscari et al., 2022) and experimental campaigns (Frederik et al., 2020b; van der Hoek et al., 2024) on wake-mixing methods observed slightly different optima in the range of $St = 0.2 - 0.4$. These previous studies indicate that the optimal frequency can depend on multiple aspects, such as the ambient conditions (e.g., wind speed, turbulence intensity), the turbine model, and the simulation environment. When adding the actuation amplitude as a control variable, one can imagine that determining the
45 optimal control settings requires a large number of computationally expensive simulations.

Although wake-mixing methods have been shown to increase the power output of a wind farm, this improvement in performance comes at the expense of increased fatigue loading (Frederik et al., 2020a). Van Vondelen et al. (2023) showed increased fatigue loads using aeroelastic simulations for a turbine applying the helix method for all components considered. Furthermore, the increase in fatigue loads was shown to be more sensitive to increasing pitch amplitudes than to actuation frequency.
50 Similar studies by Frederik and van Wingerden (2022) and Frederik et al. (2024) combining LES and aeroelastic simulations also focused on the effect of wake-mixing methods on fatigue loads of a downstream turbine. These studies showed increased loading due to the additional turbulence introduced into the wake by the periodic excitation. However, the simulations were limited to a select number of cases with fixed distance and alignment of the two turbines, and a single pitch amplitude. A more comprehensive study on the effects of wake-mixing techniques on downstream turbine loads, considering different spacing and
55 misalignment cases, is currently missing from the literature.

To assess the fatigue loading to which wind turbines are subjected under different conditions, load surrogate models offer a more efficient solution. These models are generally based on large databases of aeroelastic simulations and can predict fatigue loads based on some inflow or layout variables. Dimitrov et al. (2018) used various site-specific ambient conditions (e.g., wind speed, turbulence intensity, shear exponent, wind veer, etc.) as inputs to compare multiple surrogate models for predicting fa-



60 tigue loads. Accurate load predictions were obtained with Polynomial Chaos Expansion (PCE) and Kriging methods. However,
this database did not consider turbines operating in wake conditions. To account for wake-induced loads, a follow-up study
included additional information, consisting of turbine spacing, wake incidence angle, and the number of upstream turbines, in
the surrogate models (Dimitrov, 2019). A similar approach from Mendez Reyes et al. (2019) used wake parameters such as
65 this LUT included the effect of WFFC methods, such as wake steering and SIC, on fatigue loads. The load surrogate models
discussed so far required information on the location of a turbine with respect to the wake. More recently, several studies
presented layout-agnostic load surrogate models. Shaler et al. (2022) removed the location dependency by solely considering
several inflow statistics along different lines spanning the rotor plane to train a variety of surrogate models. Alternatively, the
rotor wind field can be reconstructed using Proper Orthogonal Decomposition (POD), which provides a reduced-order model of
70 the flow through the superposition of a selected number of modes (Liew et al., 2024). A further simplification was proposed by
Guilloré et al. (2024), who discretized the inflow (velocity and turbulence intensity) into sectors. An Artificial Neural Network
(ANN) trained with these sector-averaged inflow quantities provided accurate fatigue load estimates using only four sectors.

While some of the studies discussed in the previous paragraph evaluated the effect of WFFC on fatigue loads, the implemen-
tation of wake-mixing techniques was not included. This is primarily related to the methods for generating the load databases,
75 which rely on the combination of aeroelastic simulations to compute the turbine loads, synthetic turbulence to generate the
inflow, and engineering wake models to generate the wake inflow for downstream turbines. For example, Shaler et al. (2022)
and Guilloré et al. (2024) used FAST.FARM (Jonkman and Shaler, 2021) to obtain inputs for their load surrogate models. As
wake-mixing techniques depend on the dynamic actuation of the wake, such a simulation framework is not suitable to capture
the effects of wake-mixing control on fatigue loading.

80 This paper adds to the state-of-the-art in wake-mixing control in several ways. We present a data-driven framework based on
GP regression that models the performance of the helix method, accounting for both yield and fatigue loads. More specifically,
this framework is used to obtain the following contributions:

- Efficiently determining the optimal settings for wake-mixing techniques (i.e., the helix method) using a limited number
of LES and GP regression.
- 85 – A surrogate model for predicting WFFC fatigue loads, modeled as a GP with sector-averaged inflow quantities as pro-
posed by Guilloré et al. (2024). Inflow for the aeroelastic simulations is generated from LES to capture the periodic
nature of the wake.
- Evaluating WFFC performance in terms of energy yield and fatigue loads with the helix method on a two-turbine array
under different conditions.

90 The remainder of this paper is structured as follows. Section 2 describes the methodology, including the simulation tools
and settings, and the GP model framework. Section 3 presents the framework for efficient wake-mixing controller tuning and
its application to a two-turbine array. In Section 4, we validate the load surrogate model and test it in a case study with two
turbines. Finally, we conclude the paper with a summary and recommendations in Section 5.



2 Methodology

95 Both the wake-mixing tuning framework and the load surrogate model rely on LES. This section covers the simulation environment that was used to acquire a realistic representation of wind turbine loading and their wakes. Next, the WFFC methods that we consider for the load surrogate model are summarized. Finally, a general description of Gaussian processes is provided.

2.1 Simulation environment

100 The high-fidelity simulations that were run for this paper were performed on the Adaptive Mesh Refinement for Wind (AMR-Wind) simulator (Kuhn et al., 2025). AMR-Wind is part of the ExaWind modeling and simulation environment (Sharma et al., 2024), built on top of the AmRex library (Zhang et al., 2019). The simulator solves the three-dimensional incompressible Navier–Stokes equations in a spatially filtered resolved-scale formulation and employs the subgrid-scale one-equation turbulence model (Moeng, 1984) for smaller eddy dynamics.

2.1.1 Precursor simulations

105 Several precursor simulations of a conventionally neutral boundary layer (CNBL) were run to generate the turbulent inflow for the wind turbine simulations. We used a simulation domain of $L_x \times L_y \times L_z = 4.48 \text{ km} \times 4.48 \text{ km} \times 1.28 \text{ km}$, with 10 m equidistant cells. Coriolis forces were included, with the latitude of the domain set to $\phi_{\text{lat}} = 52.6^\circ$ to match conditions on the Dutch North Sea. For the CNBL, a potential temperature profile with an inversion height of $z_i = 700 \text{ m}$ was prescribed. The ground temperature was set to $\theta_0 = 288.15 \text{ K}$, and a capping inversion strength of $\Delta\theta = 2.5 \text{ K}$ was used over a thickness
110 of $\Delta_h = 100 \text{ m}$, followed by a lapse rate of $\gamma = 1 \text{ K km}^{-1}$. The surface roughness was set to $z_0 = 0.001$, which resulted in a turbulence intensity that varied between 3–6% over the rotor area. The resulting conditions are similar to those encountered on the North Sea (Türk and Emeis, 2010). Precursor simulations were generated for wind speeds in the range of 6–11 m s^{-1} , as this range coincides with the below-rated operating region of the turbine where WFFC is most effective. The wind direction was set to 240° (south-west), with periodic boundary conditions on the x and y boundaries. The precursors were generally
115 simulated for a period of 36,000 s to allow sufficient time for turbulence to develop and reach a quasi-steady state. After this period, the boundary conditions at the inflow boundaries are sampled for the next 70 minutes to be used later on for the turbine simulations. An example of a precursor profile is given in Figure 1, showing the prescribed temperature profile, the velocity magnitude U_∞ , turbulence intensity (TI), and wind direction (veer) ϕ as a function of height.

2.1.2 Wind turbine simulations

120 When simulating one or multiple turbines, we used the coupling between AMR-Wind and the OpenFAST aeroelastic simulator (National Renewable Energy Laboratory, 2024) to model the response of the wind turbine. The turbine model is that of the IEA 22MW reference wind turbine (Zahle et al., 2024). The turbine has a rotor diameter of $D = 284 \text{ m}$ and a hub height of $z_H = 170 \text{ m}$, with a rated wind speed of $U_{\text{rat}} = 11 \text{ m s}^{-1}$. Within the LES, the aerodynamic forces of the turbine are modeled

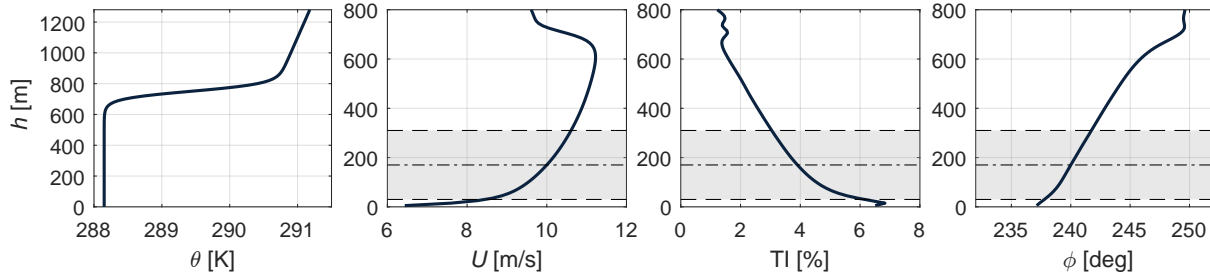


Figure 1. Average profiles of wind speed (U), turbulence intensity (I) and wind veer (ϕ) for one the precursor simulations in AMR-Wind. The dash-dotted line indicates the turbine hub-height, while the shaded areas indicate the height spanned by the wind turbine rotor.

using OpenFAST, which are subsequently applied to the incoming flow using the actuator line method (ALM). The ALM
 125 model uses 59 actuator points, matching the number of available airfoil files.

The simulation domain around the turbines was refined once to obtain cells of $\Delta x_r = 5$ m. The refinement region starts two
 diameters ($2D$) in front of the first turbine, spanning a width of $4D$, a height of $2D$, and a length of $10D$. A schematic of
 the simulation domain is provided in Figure 2. The resulting resolution in terms of rotor diameter is $D/\Delta x \approx 56$, which is
 sufficient for ALM (Martínez-Tossas et al., 2015). The blade force projection from the ALM onto the incoming flow was done
 130 with a Gaussian kernel width of $\epsilon = 2\Delta x = 10$ m to prevent numerical instabilities (Martínez et al., 2012). The LES ran with
 a constant time step of $\Delta t_{LES} = 0.05$ s, ensuring that the blades do not skip any grid cells in subsequent time steps. The time
 step of the OpenFast simulation was set to $\Delta t_{OF} = 0.01$ s. Each simulation was run for a total of 4200 s, of which the first
 600 s was used to let the wake develop and only the last 3600 s were considered for analysis. An overview of the simulation
 settings is provided in Table 1.

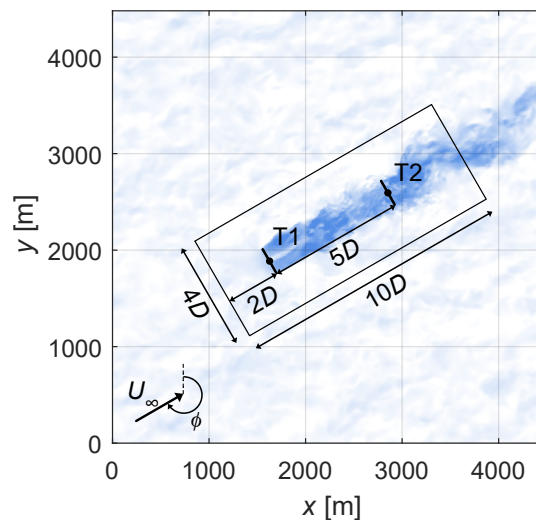


Figure 2. Schematic of the simulation setup in AMR-Wind.



Table 1. Settings for the simulations performed with AMR-Wind.

Domain settings	
Domain size	$L_x \times L_y \times L_z = 4.48 \text{ km} \times 4.48 \text{ km} \times 1.28 \text{ km}$
Cell size (base)	$\Delta x \times \Delta y \times \Delta z = 10 \text{ m} \times 10 \text{ m} \times 10 \text{ m}$
Cell size (refined)	$\Delta x_r \times \Delta y_r \times \Delta z_r = 5 \text{ m} \times 5 \text{ m} \times 5 \text{ m}$
Refinement size	$L_{x,r} \times L_{y,r} \times L_{z,r} = 2.8 \text{ km} \times 1.12 \text{ km} \times 0.6 \text{ km}$
Precursor settings	
Inversion height	$z_i = 700 \text{ m}$
Inversion strength	$\Delta\theta = 2.5 \text{ K}$
Inversion thickness	$\Delta h = 100 \text{ m}$
Lapse rate	$\gamma = 1 \text{ K km}^{-1}$
Surface roughness	$z_0 = 0.001$
Inflow wind speed	$U_\infty = 6, 8, 10, 11 \text{ m s}^{-1}$
Inflow wind direction	$\phi = 240^\circ$ (south-west)
Simulation length	$t_{\text{LES}} = 36000 \text{ s}$
Time step	$\Delta t = 0.5 \text{ s}$
Wind turbine simulations	
Simulation length	$t_{\text{LES}} = 4200 \text{ s}$
Time step LES	$\Delta t_{\text{LES}} = 0.05 \text{ s}$
Time step OpenFAST	$\Delta t_{\text{OF}} = 0.01 \text{ s}$
Turbine diameter	$D = 284 \text{ m}$
Blade epsilon	$\epsilon = 2\Delta x = 10 \text{ m}$
Rotor approximation	Actuator Line Method

135 2.2 Wind farm flow control methods

Within the simulations, the turbines were controlled using the reference open-source controller (ROSCO) toolbox for wind turbine applications (Abbas et al., 2022). In the baseline control case, the turbines were operated to maximize their own power production. The WFFC methods that are considered for the load surrogate model include wake steering and the helix method. Although we only consider these methods, the load surrogate model can easily be extended to include other strategies, such as static induction control. Implementing wake steering in the simulations is straightforward and consists of adding a constant offset to the turbine yaw angle.

In simulations of the helix control strategy, slowly varying tilt and yaw moments are imposed on the turbine. These signals are designed in a non-rotating reference frame and then translated to the rotating reference frame by using the Multi-Blade Coordinate transformation (Bir, 2008). The transformation results in individual pitch reference signals that are offset by a phase of 120° . The frequency of the pitch signals depends on the selected Strouhal number, the rotational frequency of the



turbine, and the desired direction of the helix wake (i.e., clockwise or counterclockwise):

$$f_{\beta} = f_r \pm f_e, \quad (1)$$

with the rotor frequency f_r , and the actuation frequency f_e , which depends on:

$$f_e = \frac{St \cdot U_{\infty}}{D}. \quad (2)$$

- 150 In case of the counterclockwise helix implementation, the excitation frequency is added to the rotational frequency, resulting in higher pitch rates than the clockwise version. The pitch actuation of the helix method is visualized in Figure 3. For the simulations, we use the built-in functionality of the *Active Wake Control* module in ROSCO to implement the helix approach, which requires settings for the amplitude, excitation frequency, and direction.

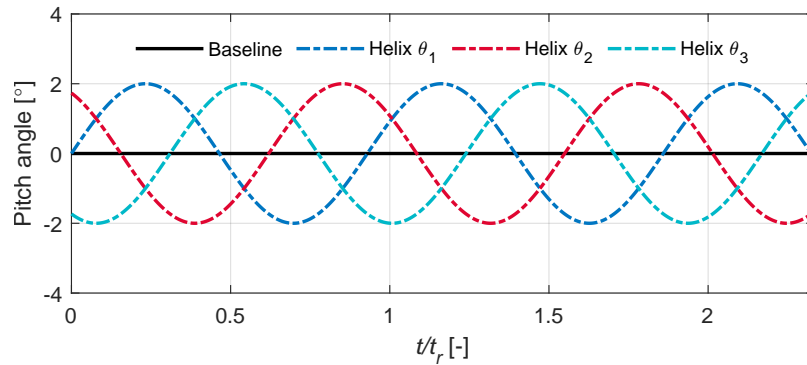


Figure 3. Example of the pitch reference signals for the counterclockwise helix. Time is normalized by the duration of one rotor rotation period $t_r = f_r^{-1}$.

2.3 Gaussian process surrogate model

- 155 The LES described in the previous sections are very computationally expensive. Each wind turbine simulation requires several days of simulation time on an HPC-cluster. Therefore, simulating a full sweep of all control parameters for the helix method becomes very time-consuming, especially when multiple ambient conditions need to be considered. When one also wants to evaluate the effects of WFFC methods on fatigue loads under different alignment and spacing conditions, simulating this becomes unfeasible. To make this problem tractable, this paper uses surrogate models trained on a limited number of LES.
- 160 The data-driven framework presented in this paper that is used to tune the helix settings and model fatigue loads is based on GP regression: (Rasmussen and Williams, 2006). When considering a GP, we assume that the output data, collected in a one-dimensional vector \mathbf{y} , belongs to a multivariate Gaussian distribution

$$\begin{bmatrix} \mathbf{y} \\ \mathbf{y}^* \end{bmatrix} \sim \mathcal{N} \left(\mathbf{0}, \begin{bmatrix} \mathbf{K}(\mathbf{x}, \mathbf{x}) + \sigma_n^2 \mathbf{I} & \mathbf{K}(\mathbf{x}, \mathbf{x}^*) \\ \mathbf{K}(\mathbf{x}^*, \mathbf{x}) & \mathbf{K}(\mathbf{x}^*, \mathbf{x}^*) \end{bmatrix} \right). \quad (3)$$



The distribution of the output depends on one or multiple inputs collected in a matrix \mathbf{x} . The vector \mathbf{y}^* refers to the inferred
165 function value for possible test inputs \mathbf{x}^* . The covariance matrix \mathbf{K} can be computed from a wide range of kernel functions
and depends on the type of function one would like to model. Two popular options are the squared exponential and Matérn
functions (Rasmussen and Williams, 2006), which will both be used in this work. Each Kernel function is equipped with a set
of hyperparameters that control the output scaling, correlation, and level of smoothness. An additional hyperparameter is given
in the form of σ_n , which represents the noise or uncertainty of the output data. In this work, the hyperparameters are obtained
170 by maximizing the log marginal likelihood. After determining the hyperparameters, we compute the posterior distribution of
the model, resulting in the mean ($\boldsymbol{\mu}^*$) and variance ($\boldsymbol{\Sigma}^*$) for the test locations (\mathbf{x}^*) using the following set of equations:

$$\boldsymbol{\mu}^* = \mathbf{K}(\mathbf{x}^*, \mathbf{x}) (\mathbf{K}(\mathbf{x}, \mathbf{x}) + \sigma_n^2 \mathbf{I})^{-1} \mathbf{y}, \quad (4)$$

$$\boldsymbol{\Sigma}^* = \mathbf{K}(\mathbf{x}^*, \mathbf{x}^*) - \mathbf{K}(\mathbf{x}^*, \mathbf{x}) (\mathbf{K}(\mathbf{x}, \mathbf{x}) + \sigma_n^2 \mathbf{I})^{-1} \mathbf{K}(\mathbf{x}, \mathbf{x}^*). \quad (5)$$

The content of the test input matrix (\mathbf{x}^*) depends on the application. When we want to determine the optimal control settings
175 for the helix method, this matrix consists of different combinations of actuation frequency and pitch amplitude. In the case of
evaluating fatigue loads, this matrix consists of the inflow conditions, as well some control inputs. Both cases will be considered
in more detail in the subsequent sections.

2.4 Load surrogate database

The workflow that is used to obtain the load surrogate model is presented in Figure 4. For each of the load channels, a separate
180 GP model is trained using the data from a loads database. This loads database is constructed using standalone aeroelastic
simulations with OpenFAST. The inflow for these simulations is taken from the LES that were run with AMR-Wind. Cross-
stream flow slices were collected at a one-second interval from the wake of a single turbine at distances between $3D$ and $8D$,
as well as a slice of the undisturbed precursor inflow. Subsequently, these time series were cut into blocks of 660 s to mimic
the effect of different turbulence seeds of the inflow conditions. Next, the flow slices were projected on a rectangular grid of
185 340 m width by 330 m height, with grid spacing of 10 m, and exported to a *.wnd* file compatible with OpenFAST. To simulate
different levels of wake overlap, a displacement parameter Δy was introduced to move the grid laterally over the cross-stream
flow slices. In this way, the aeroelastic simulations covered all wake conditions from full overlap ($\Delta y = 0$ m) to no wake
overlap ($\Delta y = \pm 390$ m).

For the LES cases, we used different control strategies, including greedy control, wake steering, and the helix method.
190 Furthermore, several simulations with three turbines were conducted to include the effect of accumulated turbulence in the
wake. An overview of all the control strategies that were simulated is provided in Table 2. The OpenFAST simulations for
the loads database also include the turbine using different control strategies to assess the impact on loads. For wake steer-
ing, the turbine was yawed with $\gamma = \{-30 : 10 : 30^\circ\}$, and for the helix method, the pitch amplitude was varied between
 $A_\beta = \{1.0 : 1.0 : 4.0^\circ\}$.

195 The entries for the load surrogate database were obtained after post-processing the time series of the inflow planes and the
load channels. The first set of inputs sent to the load surrogate model are the sector-averaged inflow quantities, as proposed by

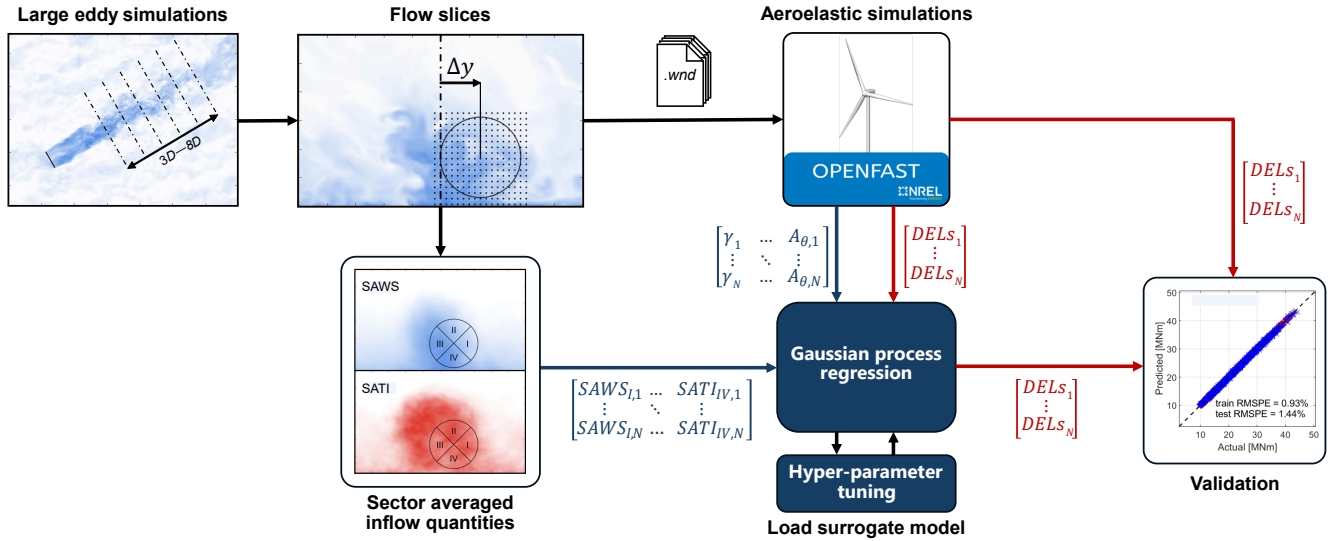


Figure 4. Schematic of the load surrogate model. Flow slices are extracted from large eddy simulations and used as inflow for aeroelastic simulations. The resulting load time series are converted into Damage Equivalent Loads and sent to a GP model along with some turbine control inputs and the sector-averaged inflow quantities. The GP model can subsequently predict fatigue loads based on a set of input conditions.

Table 2. LES cases that were run to generate the inflow for the loads database.

Simulation case	N_{WT}	Control settings
Baseline	1	$\gamma = 0^\circ, A_\beta = 0^\circ$
Helix A2	1	$\gamma = 0^\circ, A_\beta = 2^\circ$
Helix A3	1	$\gamma = 0^\circ, A_\beta = 3^\circ$
Helix A4	1	$\gamma = 0^\circ, A_\beta = 4^\circ$
Wake steering (+)	1	$\gamma = 20^\circ, A_\beta = 0^\circ$
Wake steering (-)	1	$\gamma = -20^\circ, A_\beta = 0^\circ$
Baseline array	3	$\gamma_i = [0^\circ, 0^\circ, 0^\circ], A_{\beta,i} = [0^\circ, 0^\circ, 0^\circ]$
Helix array A3	3	$\gamma_i = [0^\circ, 0^\circ, 0^\circ], A_{\beta,i} = [3^\circ, 0^\circ, 0^\circ]$
Helix array A4	3	$\gamma_i = [0^\circ, 0^\circ, 0^\circ], A_{\beta,i} = [4^\circ, 0^\circ, 0^\circ]$
Wake steering array	3	$\gamma_i = [15^\circ, 18^\circ, 0^\circ], A_{\beta,i} = [0^\circ, 0^\circ, 0^\circ]$

Guilloré et al. (2024). In this case, the inflow consisting of streamwise velocity and turbulence intensity is averaged over four sectors spanning the rotor plane. For the sector-averaged wind speed (SAWS) $U_{SA}(s)$, the wind speed value for each sector s



is determined in the following way:

$$200 \quad U_{SA}(s) = \int_{\theta=(\frac{s-1}{2}\pi - \frac{\pi}{4})}^{\theta=(\frac{s}{2}\pi - \frac{\pi}{4})} \int_{r=0}^{r=R} r \cdot u(\theta, r) dr d\theta. \quad (6)$$

In the previous equation, streamwise wind speed measurements u from the LES flow planes are integrated over the radial distance r and the azimuth angle θ , where the latter has been discretized into four sectors. The same equation is used to determine the sector-averaged turbulence intensity (SATI), where turbulence intensity is defined as:

$$TI = \frac{\sqrt{\frac{1}{3}(u'u' + v'v' + w'w')}}{U_{\infty}}. \quad (7)$$

205 Here, u' , v' , and w' indicate the instantaneous velocity deviations from the average for the streamwise, transverse, and vertical velocity components, respectively. Note that the freestream wind speed velocity U_{∞} is selected to normalize the root-mean-square of the velocity fluctuations instead of the local average wind speed. This was done to distinguish between the wake of a turbine operated with greedy control and the helix method, as the latter generally causes higher velocity fluctuations.

Next, we look at the load channels that will be used for the surrogate model. The wind turbine channels that are considered
 210 are listed in Table 3. To assess the effect of control strategies and wake conditions on the fatigue loads, time series from the load channels are converted into 1-Hz Damage Equivalent Loads (DELs) using the following equation:

$$L_{eq1Hz} = \left(\frac{\sum_{i=1}^N n_i \cdot L_i^m}{N_{cycles}} \right)^{\frac{1}{m}}. \quad (8)$$

The number of load cycles n_i and load amplitude L_i for a bin i are obtained from a standard rainflow counting algorithm for $N_{bins} = 200$. The Wöhler slope coefficient is set to $m = 10$ for the composite blades and $m = 4$ for the steel tower components.
 215 Finally, N_{cycles} refers to the number of 1 Hz cycles in the 10-minute time series, equaling a value of 600. The DEL can be interpreted as the load amplitude that does a similar amount of damage at a 1 Hz interval as the load time series.

The use of wake-mixing techniques can also have a significant impact on the blade pitch bearings due to the combination of continuous movement and alternating load cycles. One method to express the loads that the pitch bearings experience is using the Pitch Bearing Damage Equivalent Load (PBDEL) (van Vondelen et al., 2024). The PBDEL (L_{PB}) is determined using the
 220 following equation:

$$L_{PB}(\phi) = \left(\frac{\sum_{k=1}^{N_{steps}} \delta\beta(k) \cdot \max(\cos(\phi) \cdot M_{flp}(k) + \sin(\phi) \cdot M_{edg}(k), 0)^m}{N_{ref}} \right)^{\frac{1}{m}}. \quad (9)$$

The PBDELs are determined for the full range of radial positions of the bearings with 10° increments, i.e. $\phi = \{0^\circ : 10^\circ : 360^\circ\}$. The amount of pitch travel is denoted by $\delta\beta(k)$ for a time step k . The blade root flapwise and edgewise bending moments are given by M_{flp} and M_{edg} , respectively. N_{ref} indicates the reference amount of pitch travel during a 10-minute interval. In this
 225 study, we set $N_{ref} = 600^\circ$, which matches the distance a blade travels when applying the helix with an amplitude of $A_\beta = 2.0^\circ$ and with $St = 0.25$ at a wind speed of $U_{\infty} = 10 \text{ ms}^{-1}$. For the pitch bearings, a Wöhler coefficient of $m = 3$ is used (Zahle et al., 2024). For the load surrogate model, we always consider the radial position that experiences the highest load.



Table 3. List of considered wind turbine channels obtained from the OpenFAST simulations.

Channel name	Description	Units
Power	Generator power	[MW]
RotSpeed	Rotor speed	[s ⁻¹]
NacYaw	Nacelle yaw orientation	[°]
BladePitch	Blade pitch angle	[°]
RootMedg	Blade root edgewise bending moment	[MNm]
RootMflp	Blade root flapwise bending moment	[MNm]
TwrBsMxt	Tower bottom side-side bending moment	[MNm]
TwrBsMyt	Tower bottom fore-aft bending moment	[MNm]
TwrBsMzt	Tower bottom yaw moment	[MNm]
YawBrMxp	Tower top side-side bending moment	[MNm]
YawBrMyp	Tower top fore-aft bending moment	[MNm]
YarBrMzp	Tower top yaw moment	[MNm]
LSSGagMxs	Low-speed shaft torque	[MNm]
LSSGagMys	Nonrotating low-speed shaft yaw bending moment	[MNm]
LSSGagMzs	Nonrotating low-speed shaft tilt bending moment	[MNm]

3 Efficient tuning of wake-mixing control settings

This section presents the framework for tuning wake-mixing control settings. The framework uses simulations of a two-turbine array performed with AMR-Wind as presented in Section 2 using a wind speed of $U_\infty = 8$ m/s. In this case, we aim to determine the optimal pitch frequency and amplitude of the helix approach under low-turbulence conditions. However, this framework is applicable to other wake-mixing strategies and can also be expanded to include different atmospheric conditions.

3.1 Wind turbine measurements

The simulation data required for the data-driven modeling framework are extracted as time series from the OpenFAST output files. An example of such a simulation output is given in Figure 5, showing the generator power of the upstream (T1) and downstream (T2) turbines for the baseline case and the helix method. The time series show a slight decrease in power for T1, and a significant increase in power for T2, when the helix method is used. The 1-hour measurement domain is then divided into multiple 10-minute periods, and the power is averaged over time, as shown on the right-hand side of Figure 5. Note that the relative power of the helix method over the baseline can vary depending on the 10-minute time interval, due to the turbulent eddies that hit the turbines. This indicates the importance of sufficient simulation time and the use of multiple data points for a single helix case.

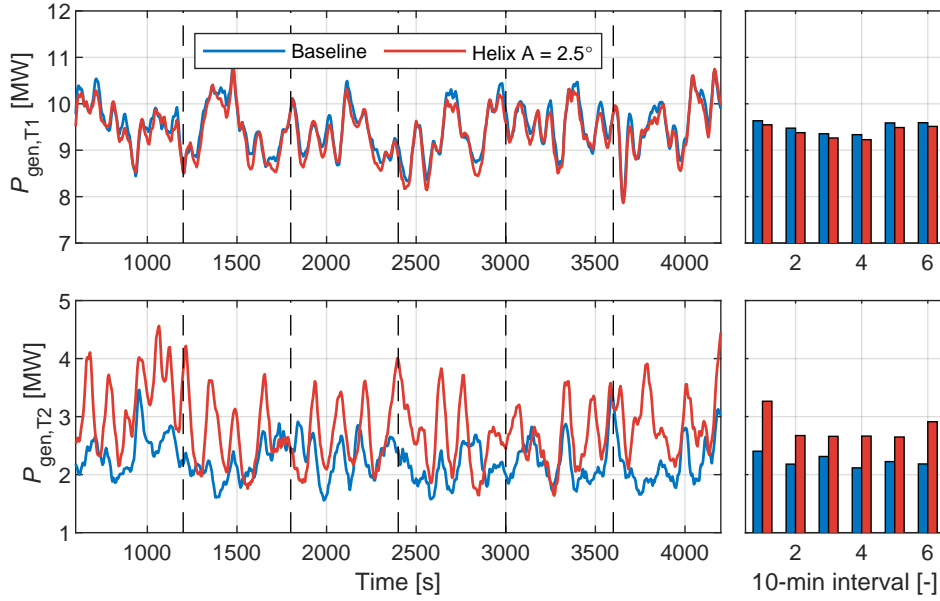


Figure 5. Power generated by the upstream (T1) and downstream (T2) turbines over time (left), and the 10-minute average power comparing baseline control to the helix method (right). The vertical dashed lines indicate the 10-minute intervals used for averaging.

The time-averaged power data is subsequently used to compute the relative power gain of the helix method over baseline control. All the relative power gain measurements are then collected and scaled to a zero mean and unity standard deviation dataset y . Similarly, we collect the training locations, consisting of the helix amplitude and frequency, in a matrix x and scale it before feeding it to the GP model as training data. For the GP to effectively identify the contribution of both turbines to the total power of the array, the model is split into two parts with their own set of hyperparameters. Hence, we obtain a GP model that estimates the power loss of T1 (μ_{T1} , σ_{T1}) due to the helix actuation, and a GP model that estimates the power gain or loss for turbine T2 (μ_{T2} , σ_{T2}) due to the affected wake recovery. A useful property of Gaussian processes is that the sum of two Gaussian processes is also a Gaussian process. Therefore, we can model the mean and variance of the total power gain as follows:

$$\mu_{\text{array}} = \mu_{T1} + \mu_{T2}, \tag{10}$$

$$\sigma_{\text{array}}^2 = \sigma_{T1}^2 + \sigma_{T2}^2, \tag{11}$$

where μ_{array} is the mean power gain of the two turbines, and σ_{array}^2 is the variance of the estimated mean power gain.

3.2 Controller tuning results

After extracting the power data from the simulations and preprocessing it, we can iteratively determine the optimal settings for the helix method for the current ambient conditions. We used a Matérn covariance function with a smoothness parameter of $\nu = 3/2$ to get a smooth but flexible model. The GP modeling framework presented in the previous section will now be used



to model the power increase of the counterclockwise (CCW) helix implementation. We first demonstrate the GP model for a fixed pitch amplitude of $A_\beta = 2.5^\circ$. Figure 6 shows the total power gain as a function of the Strouhal number. For each of the subplots, the hyperparameters are first optimised, and the mean power ratio and variance are inferred for a range of other frequencies. Based on the inferred power ratio, a new frequency is selected and subsequently applied in a new LES run, after which the process is repeated.

The model is initialised using 10-minute average data samples from three separate simulations that employed the helix method at different frequencies. For a Strouhal number just above $St = 0$, we see a power ratio below 100%, indicating a loss of power due to the actuation of the helix method. However, this ratio increases as the Strouhal number rises to values of $St = 0.2$. For the next two simulations, we focus on exploring the power ratio function by selecting Strouhal numbers of 0.5 and 1.0, respectively. Based on previous studies (Frederik et al., 2020a), we do not expect the optimal frequency to lie within this range, but we are interested in determining the shape of the function and reducing the uncertainty. After updating the GP with these simulation results, the model predicts the highest power ratios to be obtained in the range of $St = 0.2-0.4$. After the latest iteration, we notice that the GP estimates show little variation in this frequency range. The power increase for the considered pitch amplitude seems to settle at approximately 4.3%. The measurement samples also indicate that where the helix method is effective, large variations in the power ratio occur.

The next step in the modeling framework is to expand the GP model to include pitch amplitude. This requires only a small alteration to the GP model, consisting of adding an extra hyperparameter. The same approach for selecting the control settings for the LES runs is adopted as in the previous example, focusing first on exploration, followed by maximising the power gain. The final version of the GP models are presented in Figure 7 as contour maps of the power ratio as a function of frequency and pitch amplitude. From the GP model of turbine T1, we see a clear decrease in power for lower frequencies and increasing pitch amplitudes. For the second turbine, the power ratio keeps rising for increasing pitch amplitudes. When combining the models of both turbines, we obtain a contour map for the total power ratio indicating a clear optimum. The optimum indicates that at some point, the power loss of the actuated turbine (T1) can no longer be compensated by the power increase of the downstream turbine (T2). The optimal power ratio of 7.5% was achieved with an amplitude of $A_\beta = 4^\circ$ and a frequency of $St = 0.25$. While the optimal identified frequency agrees well with previous studies (Munters and Meyers, 2018b; Frederik et al., 2020a), Taschner et al. (2023) showed an increasing power trend for even higher pitch amplitudes. However, their simulations were performed with a different turbine model and for a different wind speed.

Figure 7 also shows the two-dimensional estimates of the GP models with uncertainty bounds for the optimal frequency and amplitude. The model for T1 can estimate the power loss with high certainty, with the only uncertainty arising from the lack of samples at higher frequencies. Power losses of up to 5% are visible for increasing amplitudes at the optimal frequency. The models for T2 and the overall power look very similar to each other, with higher uncertainty on the estimates. Interestingly, the range of optimal frequencies seems to narrow as the pitch amplitude increases. When operating the helix with pitch amplitudes up to 2.5° , this could offer some additional flexibility on the selected frequency. In this case, the optimal frequency is determined not only by the maximum power gain but also by the minimum fatigue loading.

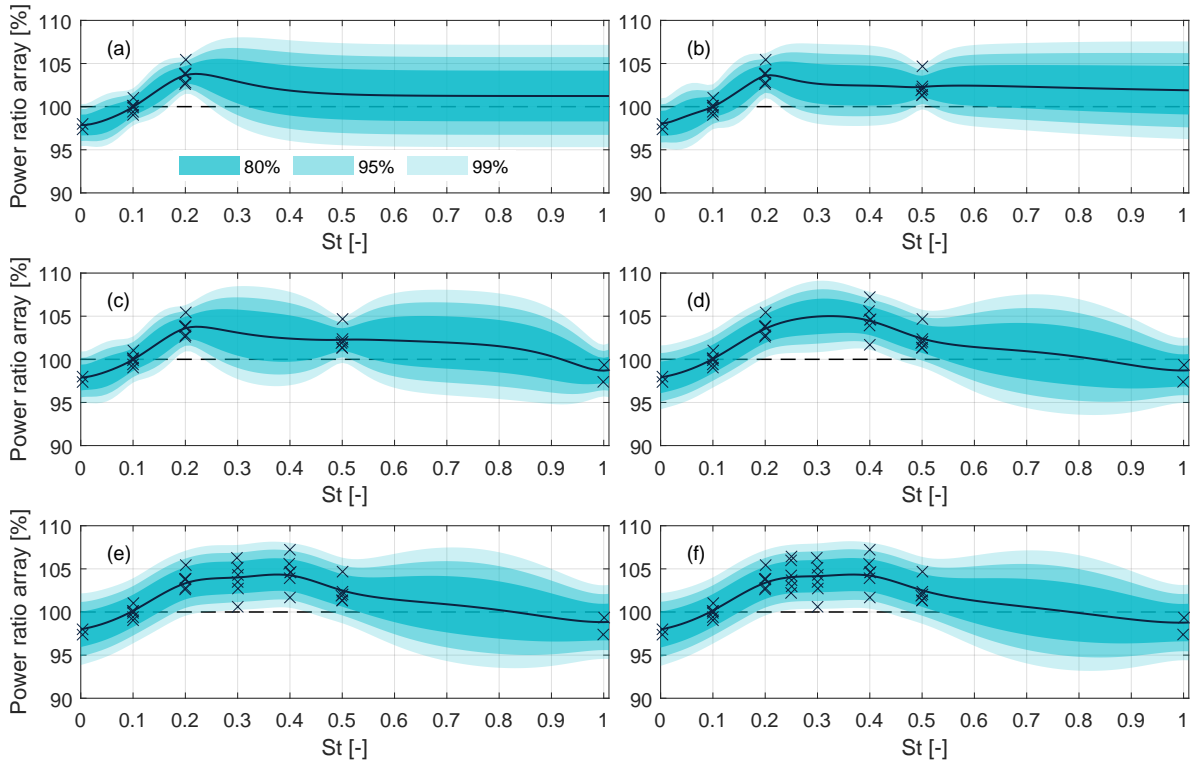


Figure 6. Power ratio of the helix method over baseline operation for the two-turbine array. Samples from the LES used to train the model are denoted by the \times -marks. The solid black line indicates the estimated power ratio of the different GP models, and the shaded areas show the uncertainty bounds of the estimated mean power. The subplots from (a)-(f) show different iterations of the GP model after additional data has been acquired.

Modeling the performance of wake-mixing techniques has thus far been limited to the CCW helix method. In Figure 8, the model is modified to include clockwise (CW) simulations of the helix method. For this model, we assume the shape of the GP model for the CW helix is similar to the CCW version. The model is therefore extended by mirroring the frequency axis to negative Strouhal numbers. Note that this refers to the contribution of the Strouhal number to the actual pitching frequency, which is given by

$$f_{\beta} = f_r + f_e = f_r + \frac{St \cdot U_{\infty}}{D}. \quad (12)$$

Here, f_{β} refers to the pitching frequency of the blades, f_r the rotational frequency of the turbine, and f_e the frequency of the helix excitation. For the CW excitation of the helix, the blade pitching frequency will be below the rotational frequency of the turbine. Figure 8 shows that the CW helix method achieves similar power gains as CCW for pitch amplitudes up to 2° . For higher pitch amplitudes, that gain remains fairly constant, which means that the power loss of the actuated turbine is not overcompensated by the power gain of the downstream turbine.

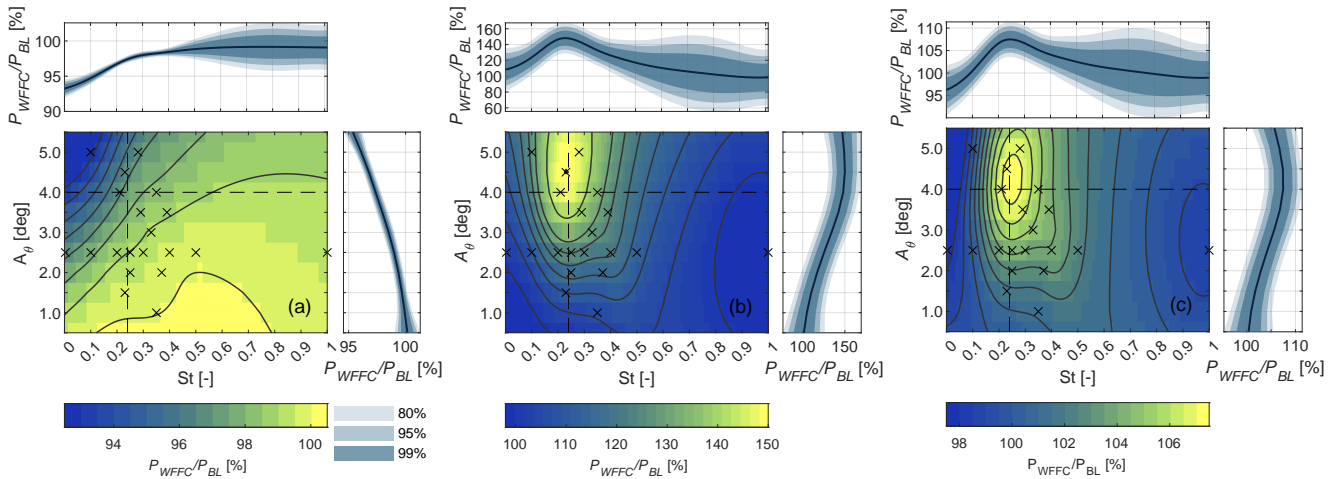


Figure 7. Power ratio of the helix method over baseline operation ($\frac{P_{WFFC}}{P_{BL}}$). The figure shows the estimated power ratio of turbine T1 (a), turbine T2 (b), and the combined power of the turbine array (c). Samples from the LES used to train the model are denoted by the \times -marks. The contour maps indicate the estimated mean power ratio of the different GP models. The dashed lines denote the optimal frequency and amplitude for the total power gain. The accompanying estimates and uncertainty bounds are shown above and to the right of the contour maps.

The tuning framework has so far been demonstrated for a single free-stream wind speed and turbulence level. However, the controller performance for additional simulation conditions could potentially be modeled by adding inputs covering wind speed, turbulence, and atmospheric stability, among others. This extension remains for future work. For the remaining contributions of this paper, the optimal controller frequency that was identified at $St = 0.25$ will be used.

4 Fatigue load prediction for wake-mixing control

This section presents the results of the load surrogate model based on the methods described in Section 2. The main purpose of the model is to predict the effect of wake-mixing methods on fatigue loading based on the rotor inflow conditions. A validation of the load surrogate model for different load channels is performed first, followed by a case study that compares different wind farm flow control strategies and their impact on turbine performance.

4.1 Surrogate model training and validation

The load database consists of 10,410 distinct simulation cases (i.e., cases with the same turbine spacing, wake overlap, and control strategy) with six turbulence seeds, resulting in 62,460 simulation results. Prior to feeding the simulation results to the GP, the results of each simulation case are averaged over the six turbulence seeds to obtain a steady-state representation of the fatigue loads. Next, the dataset is divided into a training and a test set with a 70%-30% ratio. The training set is then used

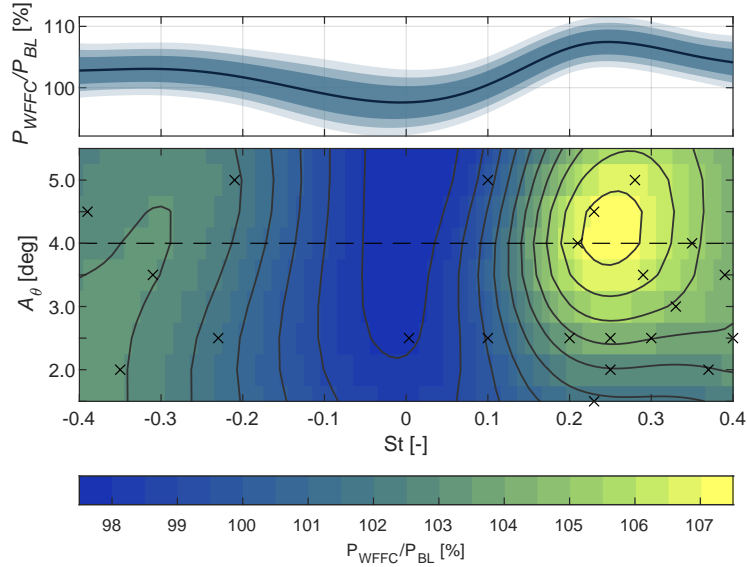


Figure 8. Power ratio of the helix method over baseline operation. The figure shows the estimated combined power of the turbine array, comparing the CW and CCW helix implementations. Samples from the LES used to train the model are denoted by the \times -marks. The dashed line denotes the optimal amplitude for the total power gain. The accompanying estimates and uncertainty bounds are shown above the contour map.

to optimise the hyperparameters of the GP as discussed in Sec. 2.3. The squared-exponential function is employed to ensure smoothness in the prediction results.

The load prediction capabilities of the load surrogate model are validated against the load database test set. From the test set, we take the sector averaged inflow quantities and control inputs and feed these as inputs to the surrogate model. The predicted load values are then compared to the test set loads. Given the large number of load channels, the validation procedure will mainly focus on four channels: the blade root flapwise bending moment (*RootMflp*), tower base fore-aft bending moment (*TwrBsMyt*), low-speed shaft yaw bending moment (*LSSGagMys*), and the pitch bearing (*PitchBr*). The validation results of the GP load surrogate model for these components are presented in Figure 9. To quantify the performance of each surrogate model, the root mean square percentage error (RMSPE) is computed for both the training and test set as:

$$\text{RMSPE} = \sqrt{\frac{1}{n} \sum_{i=1}^n \left(\frac{\hat{L}_{\text{eq1Hz},i} - L_{\text{eq1Hz},i}}{L_{\text{eq1Hz},i}} \right)^2} \cdot 100\%, \quad (13)$$

with n denoting the number of cases in the test set, and \hat{L}_{eq1Hz} the DEL prediction from the surrogate model.

For the blade root, low-speed shaft, and pitch bearing components, we observe similar prediction accuracies. In the case of the tower base, the surrogate model performs slightly worse, with some outliers visible in the higher load range. For each component, the surrogate model shows a slight decline in prediction capabilities for the test set compared to the training set, although the differences are minimal. For the remaining components, the accuracy of the surrogate models is provided in

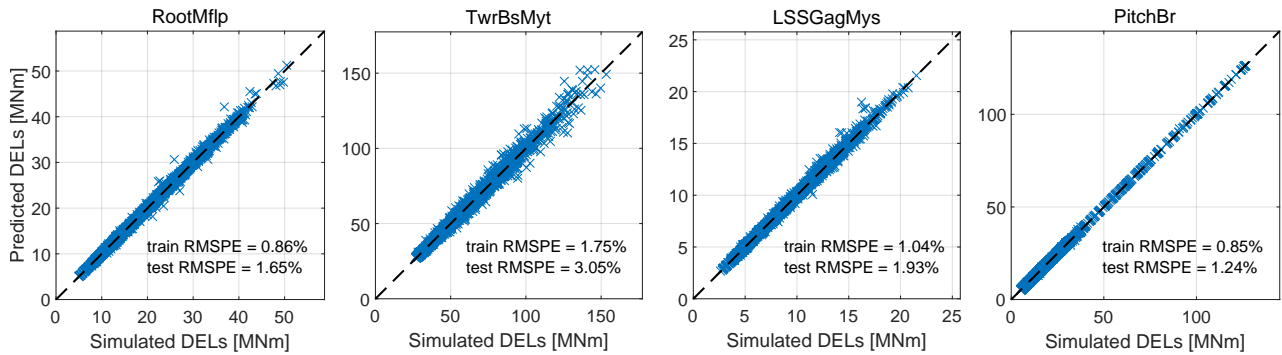


Figure 9. Scatter plots of the test data compared to predictions of the GP model based on the test input data for four of the considered structural components. The fit of the predictions for both training and test data is provided in the figure in terms of RMSPE.

335 Tab. 4. For the majority of the components, the fit with the test data is in the same range. The only outliers are the tower components in the side-side direction. The mismatch between the prediction and test data is seen primarily in the higher load range, corresponding to scenarios with full wake overlap. Adding more turbulence seeds to the loads database is expected to improve the prediction performance of the load surrogate model.

Table 4. Prediction performance of the surrogate models expressed as RMSPE for input data from the training and test sets, respectively.

Channel name	RMSPE _{train}	RMSPE _{test}
Power	0.16%	0.36%
RootMedg	0.07%	0.14%
RootMflp	0.86%	1.65%
TwrBsMxt	6.39%	8.69%
TwrBsMyt	1.75%	3.05%
TwrBsMzt	1.29%	2.47%
YawBrMxp	3.30%	4.68%
YawBrMyp	1.02%	1.90%
YarBrMzp	1.30%	2.47%
LSSGagMxs	1.46%	3.18%
LSSGagMys	1.04%	1.93%
LSSGagMzs	0.87%	1.66%
PitchBr	0.85%	1.24%



4.2 Case study

In this section, we will perform a case study featuring a two-turbine array. The upstream turbine (T1) is operating in freestream conditions, and the second turbine (T2) is located $5D$ downstream. Different control strategies will be tested on the upstream turbine, consisting of baseline (greedy) control and the helix method with different pitch amplitudes.

340 For the comparison, we used cross-stream flow slices of the streamwise velocity and turbulence intensity from the LES. An example of the flow slices is shown in Fig. 10. For T1, a flow slice of the undisturbed velocity field is selected with a hub-height velocity of $U = 10 \text{ ms}^{-1}$. This velocity field is subsequently decomposed into the four sector-averaged quantities that are used for the load surrogate model. The same approach is used for the turbulence intensity profiles. For T2, we use the flow slices extracted at $5D$ in the case when the upstream turbine is operating with baseline control, and the helix method with amplitudes
345 of $A = 2.0^\circ$ and $A = 4.0^\circ$. To replicate the effect of different alignment angles between the two turbines, we vary the lateral displacement d of the extracted rotor plane for T2.

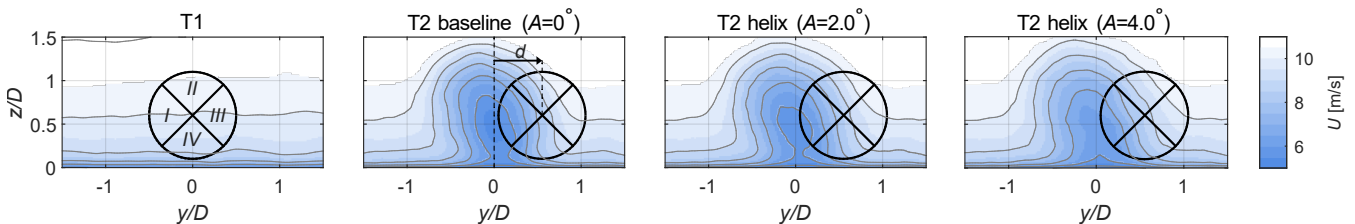


Figure 10. Example of the inflow velocity slices used for generating the load database. From left to right, we see the undisturbed inflow of T1, the inflow of T2 when T1 is using baseline control, and the inflow of T2 when T1 is using the helix method with increasing pitch amplitudes. The rotor plane is illustrated with the four sectors that are used as input for the load surrogate model.

The DELs of several components for the different cases as predicted by the load surrogate model are presented in Fig. 11. In all plots, the predictions are compared to the simulated loads from the test set and are seen to match well. The figure also contains the confidence interval of the GP's prediction. For each component, except the tower base, the surrogate model is very
350 confident of the predicted mean. Note that the confidence interval here refers to the uncertainty in the expected mean function, and does not capture the variation in loads from the different turbulence seeds.

The first column of the figure shows the effect of a rising helix pitch amplitude on the fatigue loads. All components in the figure show an increase in loads, but the most significant rise is seen for the pitch bearings. This is evident from its definition in Eq. 9, which considers the amount of travel of the bearing $\delta\beta$. For the blade root and low-speed shaft, the increase in load
355 with the helix is on the same order of magnitude as a turbine experiences when operating in a wake. Moving on to the loads of the downstream turbine (T2), we see a double Gaussian shape for the blade root bending moment when T1 uses baseline control. This load profile originates from operation with partial wake overlap, where the blades experience both high and low wind speeds over a single rotation. When the helix method is active on T1, the shape remains the same, but the peaks and the valley in the middle see a small rise for increasing pitch amplitudes. This rise can be seen as the combined result of a higher



360 wind speed and turbulence downstream with the helix. In the case of the tower base, the loads initially decrease for a helix
 amplitude of 2.0° . This results from the turbine's blade passing frequency ($3P$) coinciding with the first tower mode at lower
 wind speeds (Zahle et al., 2024). As the wind speed increases with the helix, the $3P$ frequency moves away from the tower
 mode. Then, as we apply higher pitch amplitudes, the load increases once more due to the additional turbulence in the wake.
 Both the low-speed shaft and pitch bearings see a small increase in loading with the helix method. Although for the latter, the
 365 increase in loading is insignificant when compared to the additional loading seen for T1.

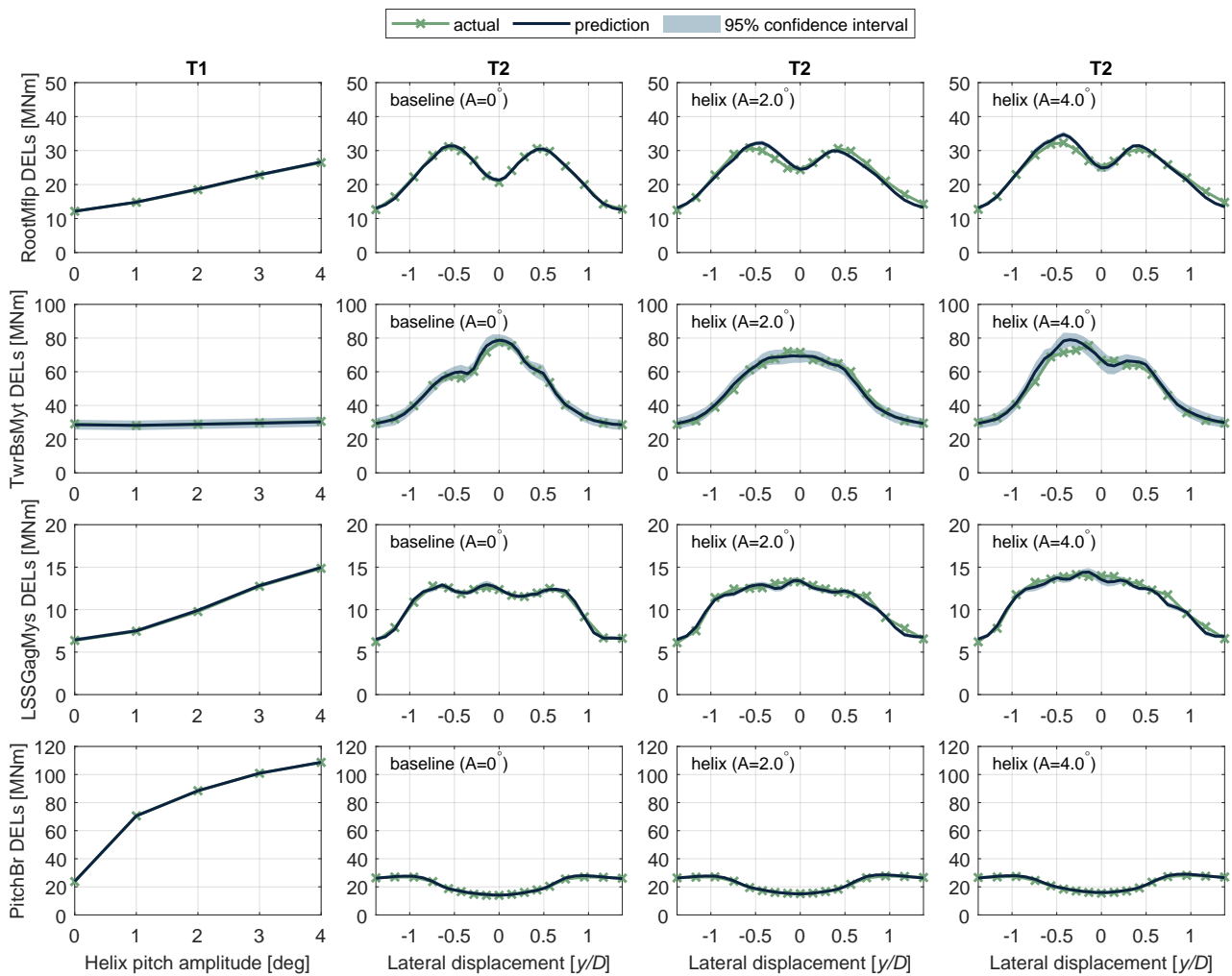


Figure 11. Comparison of loads from the simulated data against predictions from the surrogate model. The first column focuses on the effect of pitch amplitude with the helix method on loading of the upstream turbine (T1). The remaining columns consider the loads of the downstream turbine (T2) as a function of lateral displacement with respect to T1, and for different control strategies of T1. These strategies consist of baseline control, and the helix method with pitch amplitudes of $A_\beta = 2.0^\circ$ and $A_\beta = 4.0^\circ$, respectively.



Previously, we only considered the effect of the helix method on the fatigue loading of the two turbines. Similar to the various load channels, we also trained a surrogate model to predict the generator power based on the inflow sectors. In this way, we quantify the cost in terms of loads associated with a potential energy gain. For this purpose, we consider the same two-turbine array as before and evaluate the performance within a small wind direction range of $\phi = \{-4^\circ : 0.5^\circ : 4^\circ\}$ where the helix will typically be active. The helix pitch amplitude is varied between 0° and 4° . The wind direction misalignment is achieved by feeding the same angle as yaw misalignment to the surrogate models, and by displacing the incoming flow field for T2 as indicated in Fig. 10. The resulting load and power estimates are presented in Fig. 12. The average total power of the two turbines is computed for each pitch amplitude by weighting the individual estimates with a Gaussian distribution of the wind direction as proposed by Rott et al. (2018):

$$375 \quad \bar{P}_{\text{array}} = \sum_{\phi=-4^\circ}^{\phi=4^\circ} p_\phi(\phi) \cdot \hat{P}_{\text{array}}(\phi, \gamma, A_\beta). \quad (14)$$

The Gaussian distribution p_ϕ uses a standard deviation of $\sigma_\phi = 2.5^\circ$ and is discretized over the selected wind direction range with 0.5° increments. Likewise, the average DELs of each component are determined by weighting the predictions with the Gaussian distribution. Analysing the turbine array in this way replicates the effect of a realistic time-varying wind direction signal.

380 The first column in Fig. 12 shows the tradeoff in loads and power gain for the upstream turbine (T1). For the helix cases, the relative power increase is compared to the baseline case with the same wind direction misalignment. The difference in loads for each of the control cases is small, as it is primarily influenced by wind direction and thus small yaw misalignments. However, the power gain is seen to vary significantly depending on the wind direction angle. For increasing pitch amplitudes, the average power gain increases, but so do the loads of each component. The results from the downstream turbine show greater variation in terms of the loads due to the changing inflow conditions. However, the average trend is similar to that of T1 for most components. When increasing the pitch amplitude of the helix, the power gain is lifted, but at the expense of higher loading. For the blade root, tower base, and low-speed shaft, the increased loads of T1 are in the same range as those experienced by T2. Meaning that the loading of these components is dominated by wake conditions. The same does not apply to the pitch bearings, which see a large increase in loading on the actuated turbine (T1), whereas the bearings of T2 are barely affected.

390 The maximum power gain achieved in this scenario is approximately 4%, which is below the maximum gain achieved in Sec. 3.2. The difference in gain is explained by the different wind speed for this case study (i.e., $U_\infty = 10 \text{ ms}^{-1}$ instead of $U_\infty = 8 \text{ ms}^{-1}$) and the simulation environment. The latter relates to the efficiency loss the upstream turbine experiences when applying the helix. With AMR-Wind, a pitch amplitude of 4° results in a power loss of 2%, whereas the same pitch amplitude results in a power loss of 5% when simulated with standalone OpenFAST. Hence, the power loss of T1 is overestimated by the surrogate model for generator power.

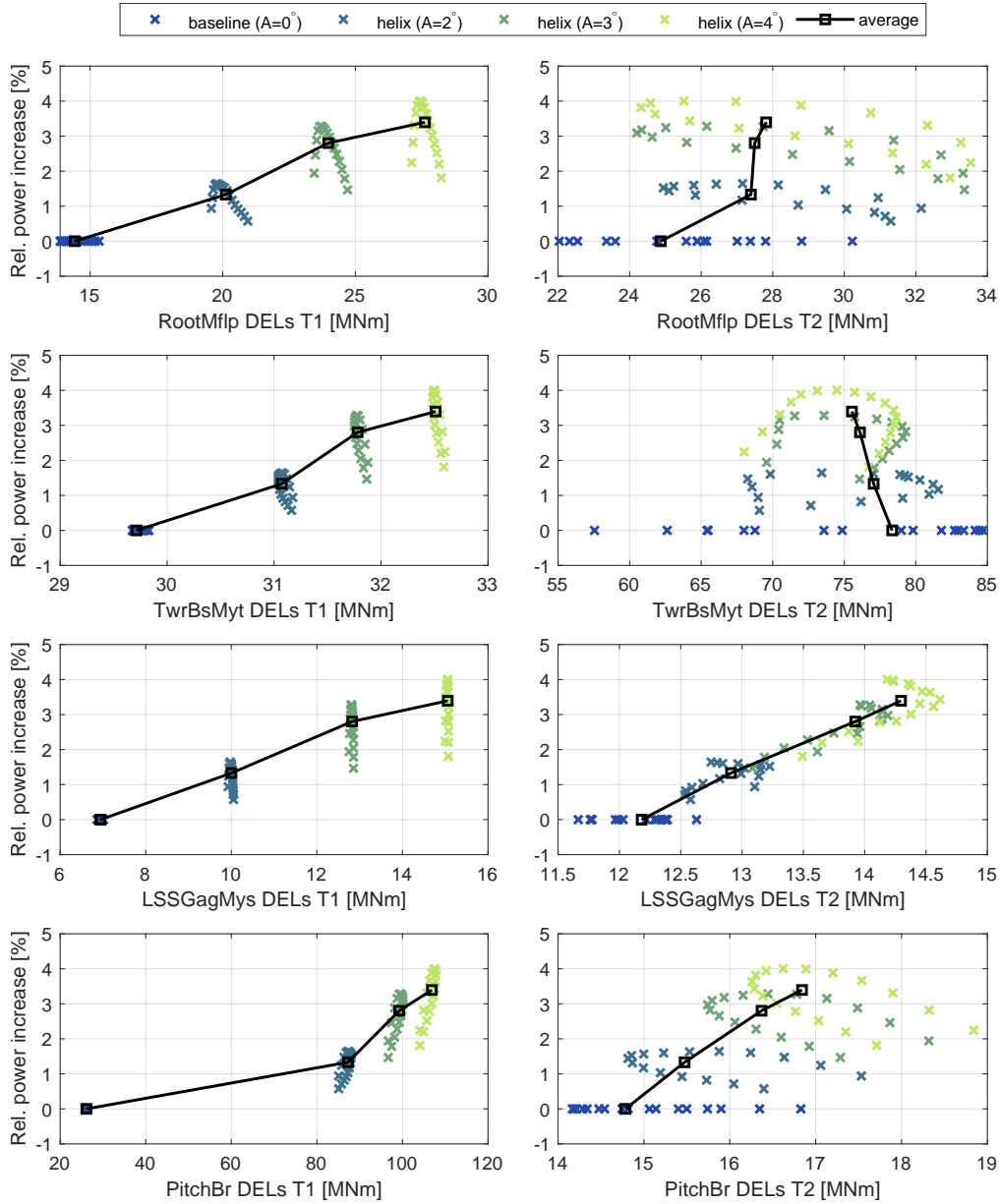


Figure 12. Tradeoff between the relative power increase and loads of a two-turbine array as predicted by the surrogate model. The left column shows the loads of T1, and the right column those of T2. The average relation between power gain and loads is determined by weighting the estimates with a Gaussian wind direction distribution.



5 Conclusions

This paper investigated the performance of the helix wake-mixing method from both yield and loading perspectives. The motivation for this work is the great computational effort required to assess these aspects, which primarily rely on large-eddy simulations. To reduce the amount of simulations and make this problem more tractable, we adopted a data-driven modeling approach with GP regression. First, the power output of a two-turbine array was modeled as a function of the actuation frequency and amplitude. The data for this model was generated with LES of the IEA22MW reference wind turbine. Second, we presented a load surrogate model for this turbine that predicts fatigue loads for wind farm flow control techniques, such as the helix method, based on the inflow and control settings.

The framework for determining optimal settings for the helix method used the power output of turbines in the large eddy simulations. These simulations were carried out with a conventionally neutral boundary layer with low turbulence levels, similar to conditions encountered on the North Sea. Time series of the turbine power were divided into ten-minute segments and averaged over these time periods. These average power measurements were then given to a GP model as training data, along with the control inputs in the form of the helix frequency (expressed as the dimensionless Strouhal number) and pitch amplitude. The training data showed the variability in power gain that wind farm flow control techniques encounter, which was also captured by the GP model in the form of prediction uncertainty. After some initial simulations with random frequencies and amplitudes to explore the control space of the model, additional simulations were performed to enhance the power yield of the two turbines. Finally, the optimal settings for this configuration and the ambient conditions were determined using a limited number of simulations. The optimal power gain of 7.5% was achieved with Strouhal number $St = 0.25$ and blade pitch amplitude $A_\beta = 4^\circ$ for the counterclockwise helix implementation. The clockwise implementation of the helix (i.e. the orientation of the wake spiral) achieved power gains of only 3%. The current framework can also be extended to include different ambient conditions, such as wind speed, turbulence intensity, and atmospheric stability conditions.

Large-eddy simulations also formed the basis of the load surrogate model presented in this paper. Building on previous work on efficient fatigue load models (e.g., Guilloré et al., 2024), a model was developed to predict the fatigue loads of the IEA22MW turbine when wake-mixing control methods, such as the helix method, are applied. Cross-stream velocity slices of turbine wakes were extracted from the LES and converted into input files for aeroelastic simulations to capture the periodic nature of the wake. This approach enabled us to simulate various levels of wake overlap and create a database comprising multiple scenarios. The time series from the aeroelastic simulations of several structural components were then processed into 1-Hz equivalent fatigue loads using a rainflow counting algorithm. The inflow was converted into four sector-averaged values for both velocity and turbulence. The sector-averaged inflow data, along with the wind farm control metrics (i.e., helix pitch amplitude and yaw misalignment angle), are used as inputs to a surrogate model based on GP regression. The load database was divided into a training and a test set, and the prediction accuracy was evaluated using the root mean square percentage error (RMSPE). For the majority of the load channels, the surrogate model achieved RMSPE levels of 3% or lower when using input data from the test dataset.



Finally, the load surrogate model was tested in a case study with two wind turbines separated by a distance of $5D$. The
430 inputs for the load surrogate model were extracted from the LES: Velocity slices of the undisturbed wind field for the upstream
turbine, and slices of the wake extracted at $5D$ for the downstream turbine. The helix method was applied on the upstream
turbine with different amplitudes ranging from $A_\beta = 0^\circ$ (baseline) to $A_\beta = 4^\circ$. For the case study, we considered several load
channels, for which the predictions agreed well with the test data. Raising the helix amplitude resulted in increased fatigue
loads for most load channels in both turbines, but most significantly in the upstream turbine. However, apart from the pitch
435 bearings, the absolute loads of the upstream turbine were of the same order of magnitude as those experienced in the wake. The
case study was concluded by evaluating the performance gain of the two turbines in terms of power yield and the additional
cost in terms of loads experienced by the turbines. For the bladeroot, tower base, and low-speed shaft components, the power
gain and increased loads appear to be well balanced. However, the pitch bearings of the upstream turbine pay a high cost for
this increase in power yield.

440 In summary, this paper employed data-driven modeling, specifically GP regression, to optimize controller settings and predict
fatigue loads using the helix wake-mixing method. Future work will focus on coupling the load surrogate model with steady-
state engineering wake models to evaluate the helix method on a wind farm level. Previous studies have investigated the
potential yield increase associated with the helix method by developing velocity deficit and added turbulence models that
depend on the helix pitch amplitude (Dammann et al., 2025a, b). However, these investigations did not consider the effect
445 of wind farm flow control methods on fatigue damage. The current study can be used to bridge this gap and account for the
increased loading during the wind farm control optimization phase, and hence achieve a balance between power gain and
increased fatigue loads.

Author contributions. DvdH: conceptualisation, methodology, software, validation, investigation, writing – original draft, visualisation. TD:
writing – review & editing, software, validation. JWvW: writing – review & editing, conceptualisation, supervision, resources, funding
450 acquisition.

Competing interests. One of the authors is an Associate editor of Wind Energy Science.

Acknowledgements. This work has been supported by the SUDOCO project, which receives the funding from the European Union's Horizon
Europe Programme under the grant No. 101122256.

The authors acknowledge the use of computational resources of the DelftBlue supercomputer, provided by Delft High Performance Comput-
455 ing Centre (<https://www.tudelft.nl/dhpc>).



References

- Abbas, N. J., Zalkind, D. S., Pao, L., and Wright, A.: A reference open-source controller for fixed and floating offshore wind turbines, *Wind Energy Science*, 7, 53–73, <https://doi.org/10.5194/wes-7-53-2022>, 2022.
- Bir, G.: Multi-blade coordinate transformation and its application to wind turbine analysis, 46th AIAA Aerospace Sciences Meeting and Exhibit, <https://doi.org/10.2514/6.2008-1300>, 2008.
- 460 Dammann, T., van der Hoek, D., Yu, W., and van Wingerden, J. W.: Enhanced Wind Farm Performance via Active Wake Control: A Steady-State Approach, 2025 American Control Conference (ACC), pp. 2856–2861, <https://doi.org/10.23919/ACC63710.2025.11107695>, 2025a.
- Dammann, T., van der Hoek, D. C., Yu, W., and van Wingerden, J. W.: A Novel Engineering Wake Model for Helix-Actuated Wind Turbine Wakes, SSRN, <https://doi.org/10.2139/SSRN.5765915>, 2025b.
- 465 Dimitrov, N.: Surrogate models for parameterized representation of wake-induced loads in wind farms, *Wind Energy*, 22, 1371–1389, <https://doi.org/10.1002/WE.2362>, 2019.
- Dimitrov, N., Kelly, M. C., Vignaroli, A., and Berg, J.: From wind to loads: Wind turbine site-specific load estimation with surrogate models trained on high-fidelity load databases, *Wind Energy Science*, 3, 767–790, <https://doi.org/10.5194/WES-3-767-2018>, 2018.
- Fleming, P. A., Gebraad, P. M., Lee, S., van Wingerden, J. W., Johnson, K., Churchfield, M., Michalakes, J., Spalart, P., and Moriarty, P.: Evaluating techniques for redirecting turbine wakes using SOWFA, *Renewable Energy*, 70, 211–218, <https://doi.org/10.1016/j.renene.2014.02.015>, 2014.
- 470 Frederik, J. A. and van Wingerden, J. W.: On the load impact of dynamic wind farm wake mixing strategies, *Renewable Energy*, 194, 582–595, <https://doi.org/10.1016/J.RENENE.2022.05.110>, 2022.
- Frederik, J. A., Doekemeijer, B. M., Mulders, S. P., and van Wingerden, J. W.: The helix approach: using dynamic individual pitch control to enhance wake mixing in wind farms, *Wind Energy*, <https://doi.org/10.1002/we.2513>, 2020a.
- 475 Frederik, J. A., Weber, R., Cacciola, S., Campagnolo, F., Croce, A., Bottasso, C., and van Wingerden, J. W.: Periodic dynamic induction control of wind farms: proving the potential in simulations and wind tunnel experiments, *Wind Energy Science*, 5, 245–257, <https://doi.org/10.5194/wes-5-245-2020>, 2020b.
- Frederik, J. A., Simley, E., Brown, K. A., Yalla, G. R., Cheung, L. C., and Fleming, P. A.: Comparison of wind-farm control strategies under realistic offshore wind conditions: turbine quantities of interest, *Wind Energy Science Discussions*, <https://doi.org/10.5194/WES-2024-164>, 2024.
- 480 Gebraad, P. M. O., Teeuwisse, F. W., van Wingerden, J. W., Fleming, P. A., Ruben, S. D., Marden, J. R., and Pao, L. Y.: Wind plant power optimization through yaw control using a parametric model for wake effects-a CFD simulation study, *Wind Energy*, 19, 95–114, <https://doi.org/10.1002/we.1822>, 2016.
- 485 Guilloré, A., Campagnolo, F., and Bottasso, C. L.: A control-oriented load surrogate model based on sector-averaged inflow quantities: capturing damage for unwaked, waked, wake-steering and curtailed wind turbines, *Journal of Physics: Conference Series*, 2767, 032019, <https://doi.org/10.1088/1742-6596/2767/3/032019>, 2024.
- Jonkman, J. and Shaler, K.: FAST.Farm User’s Guide and Theory Manual, <https://research-hub.nrel.gov/en/publications/fastfarm-users-guide-and-theory-manual>, 2021.
- 490 Kanev, S., Savenije, F., and Engels, W.: Active wake control: An approach to optimize the lifetime operation of wind farms, *Wind Energy*, 21, 488–501, <https://doi.org/10.1002/we.2173>, 2018.



- Kuhn, M., Henry de Frahan, M., Mohan, P., Deskos, G., Churchfield, M., Cheung, L., Sharma, A., Almgren, A., Ananthan, S., Brazell, M., Martínez-Tossas, L., Thedin, R., Rood, J., Sakievich, P., Vijayakumar, G., Zhang, W., and Sprague, M.: AMR-Wind: A Performance-Portable, High-Fidelity Flow Solver for Wind Farm Simulations, *Wind Energy*, 28, <https://doi.org/10.1002/WE.70010>, 2025.
- 495 Liew, J., Riva, R., Friis-Møller, M., and Gocmen, T.: Wind Farm Control Optimisation Under Load Constraints Via Surrogate Modelling, in: *Journal of Physics: Conference series*, vol. 2767, <https://doi.org/10.1088/1742-6596/2767/9/092039>, 2024.
- Martínez, L. A., Leonardi, S., Churchfield, M. J., and Moriarty, P. J.: A comparison of actuator disk and actuator line wind turbine models and best practices for their use, 50th AIAA Aerospace Sciences Meeting Including the New Horizons Forum and Aerospace Exposition, <https://doi.org/10.2514/6.2012-900>, 2012.
- 500 Martínez-Tossas, L. A., Churchfield, M. J., and Leonardi, S.: Large eddy simulations of the flow past wind turbines: actuator line and disk modeling, *Wind Energy*, 18, 1047–1060, <https://doi.org/10.1002/WE.1747>, 2015.
- Mendez Reyes, H., Kanev, S., Doekemeijer, B., and Van Wingerden, J. W.: Validation of a lookup-table approach to modeling turbine fatigue loads in wind farms under active wake control, *Wind Energy Science*, 4, 549–561, <https://doi.org/10.5194/WES-4-549-2019>, 2019.
- Meyers, J., Bottasso, C., Dykes, K., Fleming, P., Gebraad, P., Giebel, G., Göçmen, T., and van Wingerden, J.-W.: Wind farm flow control: prospects and challenges, *Wind Energy Science*, 7, 2271–2306, <https://doi.org/10.5194/wes-7-2271-2022>, 2022.
- 505 Moeng, C.-H.: A Large-Eddy-Simulation Model for the Study of Planetary Boundary-Layer Turbulence, *Journal of Atmospheric Sciences*, 41, 2052 – 2062, [https://doi.org/10.1175/1520-0469\(1984\)041<2052:ALESMF>2.0.CO;2](https://doi.org/10.1175/1520-0469(1984)041<2052:ALESMF>2.0.CO;2), 1984.
- Munters, W. and Meyers, J.: Dynamic Strategies for Yaw and Induction Control of Wind Farms Based on Large-Eddy Simulation and Optimization, *Energies* 2018, Vol. 11, Page 177, 11, 177, <https://doi.org/10.3390/EN11010177>, 2018a.
- 510 Munters, W. and Meyers, J.: Towards practical dynamic induction control of wind farms: Analysis of optimally controlled wind-farm boundary layers and sinusoidal induction control of first-row turbines, *Wind Energy Science*, 3, 409–425, <https://doi.org/10.5194/WES-3-409-2018>, 2018b.
- Muscari, C., Schito, P., Viré, A., Zasso, A., van der Hoek, D., and van Wingerden, J. W.: Physics informed DMD for periodic Dynamic Induction Control of Wind Farms, *Journal of Physics: Conference Series*, 2265, 022 057, <https://doi.org/10.1088/1742-6596/2265/2/022057>, 2022.
- 515 National Renewable Energy Laboratory: OpenFAST: Open-source wind turbine simulation tool, <https://github.com/OpenFAST/openfast>, accessed: 2024-09-26, 2024.
- NREL: FLORIS., GitHub repository, <https://github.com/NREL/floris>, 2024.
- Pedersen, M. M., Forsting, A. M., van der Laan, P., Riva, R., Romàn, L. A. A., Risco, J. C., Friis-Møller, M., Quick, J., Christiansen, J. P. S., Rodrigues, R. V., Olsen, B. T., and Réthoré, P.-E.: PyWake 2.5.0: An open-source wind farm simulation tool, <https://gitlab.windenergy.dtu.dk/TOPFARM/PyWake>, 2023.
- 520 Rasmussen, C. E. and Williams, C. K. I.: Rasmussen and Williams - Gaussian Processes for Machine Learning, ISBN 026218253X, <https://doi.org/10.1142/S0129065704001899>, 2006.
- Rott, A., Doekemeijer, B., Seifert, J. K., van Wingerden, J.-W., and Kühn, M.: Robust active wake control in consideration of wind direction variability and uncertainty, *Wind Energy Science*, 3, 869–882, <https://doi.org/10.5194/wes-3-869-2018>, 2018.
- 525 Shaler, K., Jasa, J., and Barter, G. E.: Efficient Loads Surrogates for Waked Turbines in an Array , *Journal of Physics: Conference Series*, 2265, 32 095, <https://doi.org/10.1088/1742-6596/2265/3/032095>, 2022.
- Sharma, A., Brazell, M. J., Vijayakumar, G., Ananthan, S., Cheung, L., deVelder, N., Henry de Frahan, M. T., Matula, N., Mul-lowney, P., Rood, J., Sakievich, P., Almgren, A., Crozier, P. S., and Sprague, M.: ExaWind: Open-source CFD for hybrid-



- 530 RANS/LES geometry-resolved wind turbine simulations in atmospheric flows, *Wind Energy*, 27, 225–257, <https://doi.org/https://doi-org.tudelft.idm.oclc.org/10.1002/we.2886>, 2024.
- Taschner, E., van Vondelen, A. A. W., Verzijlbergh, R., and van Wingerden, J. W.: On the performance of the helix wind farm control approach in the conventionally neutral atmospheric boundary layer, *Journal of Physics: Conference Series*, 2505, 12 006, <https://doi.org/10.1088/1742-6596/2505/1/012006>, 2023.
- 535 Türk, M. and Emeis, S.: The dependence of offshore turbulence intensity on wind speed, *Journal of Wind Engineering and Industrial Aerodynamics*, 98, 466–471, <https://doi.org/10.1016/J.JWEIA.2010.02.005>, 2010.
- van der Hoek, D., Kanev, S., Allin, J., Bieniek, D., and Mittelmeier, N.: Effects of axial induction control on wind farm energy production - A field test, *Renewable Energy*, 140, 994–1003, <https://doi.org/10.1016/j.renene.2019.03.117>, 2019.
- van Vondelen, A. A., Navalkar, S. T., Kerssemakers, D. R., and van Wingerden, J. W.: Enhanced wake mixing in wind farms using the Helix approach: A loads sensitivity study, 2023 American Control Conference (ACC), pp. 831–836, <https://doi.org/10.23919/ACC55779.2023.10155965>, 2023.
- 540 van Vondelen, A. A., Pamososuryo, A. K., Navalkar, S. T., and van Wingerden, J. W.: Control of Periodically Waked Wind Turbines, *IEEE Transactions on Control Systems Technology*, <https://doi.org/10.1109/TCST.2024.3508577>, 2024.
- van der Hoek, D., den Abbeele, B. V., Simao Ferreira, C., and van Wingerden, J. W.: Maximizing wind farm power output with the helix approach: Experimental validation and wake analysis using tomographic particle image velocimetry, *Wind Energy*, <https://doi.org/10.1002/WE.2896>, 2024.
- 545 Zahle, F., Barlas, A., Lønbæk, K., Bortolotti, P., Zalkind, D., Wang, L., Labuschagne, C., Sethuraman, L., and Barter, G.: Definition of the IEA Wind 22-Megawatt Offshore Reference Wind Turbine, Tech. Rep. DTU Wind Report E-0243, <https://doi.org/10.11581/DTU.00000317>, Technical University of Denmark, International Energy Agency, 2024.
- 550 Zhang, W., Almgren, A., Beckner, V., Bell, J., Blaschke, J., Chan, C., Day, M., Friesen, B., Gott, K., Graves, D., Katz, M., Myers, A., Nguyen, T., Nonaka, A., Rosso, M., Williams, S., and Zingale, M.: AMReX: a framework for block-structured adaptive mesh refinement, *Journal of Open Source Software*, 4, 1370, <https://doi.org/10.21105/joss.01370>, 2019.